Astronomy & Astrophysics manuscript no. i20293_astroph
January 18, 2007

Star formation in a clustered environment around the UCH II region in IRAS 20293+3952

A. Palau[1], R. Estalella[1], J. M. Girart[2], P. T. P. Ho[3], Q. Zhang[3], & H. Beuther[4]

[1] Departament d'Astronomia i Meteorologia, Universitat de Barcelona, Av. Diagonal 647, 08028 Barcelona, Catalunya, Spain
[2] Institut de Ciències de l'Espai (CSIC-IEEC), Campus UAB, Facultat de Ciències, Torre C5-Parell-2a, 08193 Bellaterra, Catalunya, Spain
[3] Harvard-Smithsonian Center for Astrophysics, 60 Garden Street, Cambridge, MA 02138, USA
[4] Max-Planck-Institut for Astronomy, Koenigstuhl 17, 69117 Heidelberg, Germany

Received / Accepted

ABSTRACT

Aims. We aim at studying the cluster environment surrounding the UCH II region in IRAS 20293+3952, a region in the first stages of formation of a cluster around a high-mass star.
Methods. BIMA and VLA were used to observe the 3 mm continuum, N_2H^+ (1–0), NH_3 (1,1), NH_3 (2,2), and CH_3OH (2–1) emission of the surroundings of the UCH II region. We studied the kinematics of the region and computed the rotational temperature and column density maps by fitting the hyperfine structure of N_2H^+ and NH_3.
Results. The dense gas traced by N_2H^+ and NH_3 shows two different clouds, a main cloud to the east of the UCH II region, of ∼0.5 pc and ∼250 $M_\odot$, and a western cloud, of ∼0.15 pc and ∼30 $M_\odot$. The dust emission reveals two strong components in the northern side of the main cloud, BIMA 1 and BIMA 2, associated with YSOs driving molecular outflows, and two fainter components in the southern side, BIMA 3 and BIMA 4, with no signs of star forming activity. Regarding the CH_3OH, we found strong emission in a fork-like structure associated with outflow B, as well as emission associated with outflow A. The YSOs associated with the dense gas seem to have a diversity of age and properties. The rotational temperature is higher in the northern side of the main cloud, around 22 K, where there are most of the YSOs, than in the southern side, around 16 K. There is strong chemical differentiation in the region, since we determined low values of the NH_3/N_2H^+ ratio, ∼50, associated with YSOs in the north of the main cloud, and high values, up to 300, associated with cores with no detected YSOs, in the south of the main cloud. Such a chemical differentiation is likely due to abundance/depletion effects. Finally, interaction between the different sources in the region is important. First, the UCH II region is interacting with the main cloud, heating it and enhancing the CN (1–0) emission. Second, outflow A seems to be excavating a cavity and heating its walls. Third, outflow B is interacting with the BIMA 4 core, likely producing the deflection of the outflow and illuminating a clump located ∼0.2 pc to the northeast of the shock.
Conclusions. The star formation process in IRAS 20293+3952 is not obviously associated with interactions, but seems to take place where density is highest.

Key words. Stars: formation — ISM: individual: IRAS 20293+3952 — ISM: dust — ISM: clouds

1. Introduction

It is generally accepted that the formation of massive stars takes place not isolated but simultaneously with the formation of a cluster. Clusters of infrared sources have been studied at optical and near-infrared wavelengths around intermediate/high-mass stars (e.g., McCaughrean & Stauffer 1994; Hillenbrand 1995; Hillenbrand & Hartmann 1998; Testi et al. 1998, 1999, 2000). One could surmise on the structure and the evolutionary state of the molecular cloud when such clusters were being born around an intermediate/high-mass protostar. In the standard theory of star formation, the central massive object, deeply embedded in large amounts of gas and dust, starts to radiate at UV wavelengths at very early stages, before finishing the accretion of all its final mass (e. g., Bernasconi & Maeder 1996). The UV photons ionize the surrounding medium, and the high-mass star developes an UCH II region around it (see, eg. Garay & Lizano 1999), which expands and pushes forward the gas and dust surrounding it until the parental cloud is completely disrupted and a cluster of infrared/optical sources emerges (e. g., Hester & Desch 2005). The study of the clumpy medium around massive protostars helps not only in the understanding of the formation of the massive star itself, but also provides a direct way to study the clustered mode of star formation, in which most stars are thought to form.

In order to properly characterize the medium around a massive protostar, it is necessary to be sensitive to small (∼2000 AU) and low-mass ($\lesssim 1\ M_\odot$) clumps of gas and dust. For this, interferometric observations toward relatively nearby (< 3 kpc) massive star-forming regions are required, and are now possible with sufficient sensitivity. Here we report on observations of one intermediate/high-mass star-forming region, IRAS 20293+3952, located at 2.0 kpc of distance (Beuther et al. 2004b) in the south-western edge of the Cygnus OB2 association, and with a luminosity of 6300 $L_\odot$. This region has been included in the sample of high-mass protostar candidates of Sridharan et al. (2002). The IRAS source is associated with the only centimeter source detected in the region, which is likely tracing an UCH II region (Beuther et al. 2002b). A study of the H_2 emission in the region shows two near-infrared stars (IRS 1 and IRS 2) associated

Send offprint requests to: Aina Palau,
e-mail: apalau@am.ub.es

with the IRAS source, and a circular ring of H_2 emission surrounding IRS 1 (Kumar et al. 2002). Beuther et al. (2002a) observed the region with the IRAM 30 m telescope and find some substructure at 1.2 mm around the UCH II region. The strongest millimeter peak, very close to the position of a H_2O maser, is located ∼15″ north-east of the IRAS source, and observations with high angular resolution by Beuther et al. (2004a) reveal a compact and strong millimeter source, mm1, associated with the H_2O maser. Two other fainter compact millimeter sources, mm2 and mm3, are located 10″ to the east of the UCH II region. Beuther et al. (2004a), from CO (2–1) and SiO (2–1) observations, suggest the presence of four molecular outflows in the region, with two of them, outflows A and B, associated with two chains of H_2 knots (Kumar et al. 2002). Subsequent observations with the PdBI were carried out at 2.6 and 1.3 mm by Beuther et al. (2004b), who find CN emission close to mm1, mm2 and mm3. The different millimeter sources detected and the presence of multiple outflows around the UCH II region makes this region a good choice to study star formation and interaction in a clustered environment.

In this paper we report on BIMA and VLA observations of the continuum at 3 mm and the dense gas traced by N_2H^+ (1–0), NH_3 (1,1), and NH_3 (2,2) toward IRAS 20293+3952, together with observations of several CH_3OH (2–1) transitions. In § 2 we summarize the observations and the reduction process, in § 3 we show the main results for the continuum and molecular line emission, in § 4 we analyze the line emission and show the method used to derive the rotational temperature and column density maps. Finally, in § 5 we discuss the results obtained, mainly the properties of the dense gas surrounding the UCH II region, the different sources identified in the region, and the interaction between them.

2. Observations

2.1. BIMA

The N_2H^+ (1–0) and CH_3OH (2–1) lines and continuum at 95 GHz were observed towards the IRAS 20293+3952 region with the BIMA array[1] at Hat Creek. The observations were carried out on 2003 September 28 in the C configuration, and on 2004 March 24, in the B configuration, with 10 antennas in use. The phase center of the observations was set at $\alpha(J2000) = 20^h31^m12\overset{s}{.}70$; $\delta(J2000) = +40°03'13\overset{''}{.}4$ (position of the millimeter peak detected with the IRAM 30 m telescope by Beuther et al. 2002a). The full range of projected baselines, including both configurations, was 9.4–240 m. The FWHM of the primary beam at the frequency of the observations was ∼120″. Typical system temperatures were ∼500 K for Sep 28 and 500–1500 K for Mar 24.

The digital correlator was configured to observe simultaneously the continuum emission, the N_2H^+ (1–0) group of hyperfine transitions (93.17631 GHz, in the lower sideband), and the CH_3OH 2_1–1_1 E, 2_0–1_0 E, 2_0–1_0 A^+, and 2_{-1}–1_{-1} E transitions (96.74142 GHz, in the upper sideband). For the continuum, we used a bandwidth of 600 MHz in each sideband, and for the lines we used a bandwidth of 25 MHz with 256 channels of 100 kHz width, providing a spectral resolution of 0.31 km s^{-1}.

Phase calibration was performed with QSO 2013+370, with typical rms in the phases of 12° and 43° for C and B configurations, respectively. The absolute position accuracy was estimated to be around 0.″5. We also used QSO 2013+370 for flux calibration, and the error in the flux density scale was assumed to be ∼30%. Data were calibrated and imaged using standard procedures in MIRIAD (Sault et al. 1995). We combined the data from B and C configurations. In order to improve the angular resolution of the continuum emission, we weighted the visibility data with a robust parameter of +1. For the line emission, which is more extended than the continuum, we used natural weighting. The resulting synthesized beams and the final rms noises are listed in Table 1.

2.2. VLA

Observations of the $(J, K) = (1, 1)$ and $(2, 2)$ inversion transitions of the ammonia molecule were carried out with the Very Large Array (VLA) of the NRAO[2] in the D configuration on 2000 September 3. The phase center was set to $\alpha(J2000) = 20^h31^m10\overset{s}{.}70$; $\delta(J2000) = +40°03'10\overset{''}{.}7$ (catalogue position of the IRAS source). The FWHM of the primary beam at the frequency of observation was ∼110″, and the range of projected baselines was 37.9–708 m. The absolute flux calibration was performed by using 3C 48, adopting a flux density at 1.3 cm of 1.05 Jy. The phase calibrator was QSO 2013+370, with a 1.3 cm bootstrapped flux density of 3.84 Jy, and 3C 84 was used as the bandpass calibrator.

The NH_3 (1,1) and NH_3 (2,2) lines were observed simultaneously in the 4 IF correlator mode of the VLA (with 2 polarizations for each line), providing 63 channels with a spectral resolution of 0.62 km s^{-1} across a bandwidth of 3.13 MHz, plus an additional continuum channel containing the central 75% of the total bandwidth. The bandwidth was centered at the systemic velocity v_{LSR} = 6.3 km s^{-1} (Sridharan et al. 2002) for the NH_3 (1,1) line, and at v_{LSR} = 11.3 km s^{-1} for the NH_3 (2,2) line (to cover the main and one of the satellite components). Data were calibrated and imaged using standard procedures of AIPS. The cleaned channel maps were made using natural weighting of the visibility data. Table 1 summarizes the parameters of the observations.

3. Results

3.1. Continuum emission

Figure 1 shows the continuum map at 3.15 mm overlaid on the continuum infrared emission at 2.12 μm from Kumar et al. (2002). The millimeter continuum emission has two strong components, BIMA 1 and BIMA 2, both spatially resolved. While BIMA 1 is elongated in a northeast-southwest direction (roughly P.A.≃45°), BIMA 2 is somewhat flattened in the east-west direction, and is surrounded by an elongated structure of ∼30″ (0.3 pc), which is tracing a dust ridge. There is an extended clump 10″ to the southeast of the dust ridge, which we label BIMA 3. Note that in this southeastern region there are very few infrared sources. At 10″ to the east of the ridge, there is another faint feature, BIMA 4, extending for 10″ in the northwest-southeast direction. Continuum emission at a level of 5σ is detected toward the position of the UCH II region, and toward IRS 2. Beuther et al. (2004b) observed the same region at 2.6 mm with the PdBI at higher angular resolution (1.″5×1.″2), but with a smaller primary beam (44″). The authors find a very strong compact source, mm1, toward the position of BIMA 1 and elongated

[1] The BIMA array was operated by the Berkeley-Illinois-Maryland Association with support from the National Science Foundation.

[2] The National Radio Astronomy Observatory is a facility of the National Science Foundation operated under cooperative agreement by Associated Universities, Inc.

Table 1. Parameters of the BIMA and VLA observations

Observation	Telescope	Config.	Beam (arcsec)	P.A. (°)	Spec. resol. (km s^{-1})	Rms[a] (mJy beam^{-1})
Continuum	BIMA	B+C	5.8×5.6	−6.4	–	0.7
CH_3OH (2–1)	BIMA	B+C	6.1×5.7	−6.2	0.31	80
N_2H^+ (1–0)	BIMA	B+C	6.2×5.9	−4.1	0.31	70
NH_3 (1,1)	VLA	D	6.9×3.0	71.5	0.62	3
NH_3 (2,2)	VLA	D	6.6×3.1	71.4	0.62	3

[a] Rms noise per channel in the case of line emission.

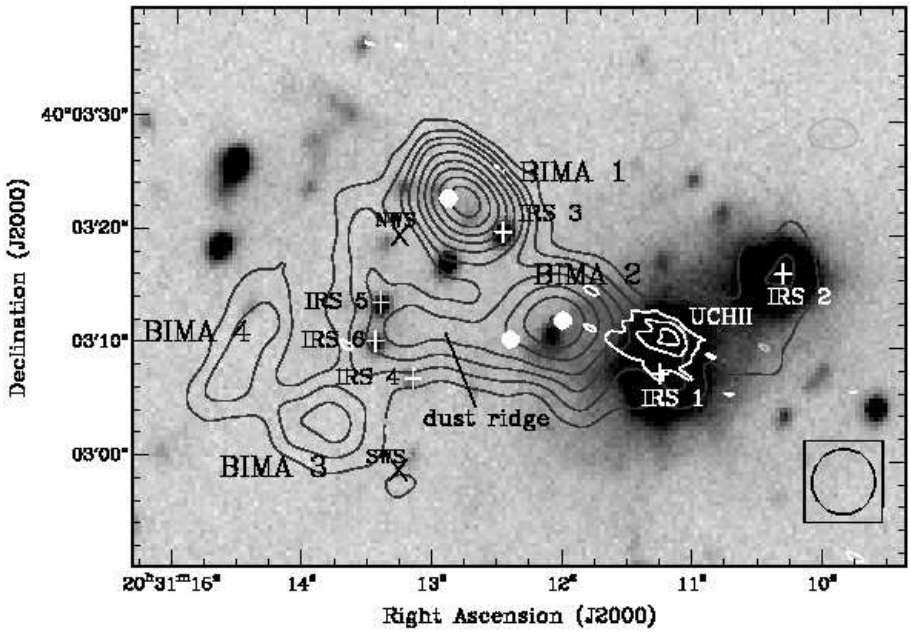

Fig. 1. Contours: 3.15 mm continuum emission from IRAS 20293+3952 obtained with BIMA in the B and C configurations using an intermediate weight between uniform and natural (robust = +1). The contour levels are −3, 3, 5, 7, 9, 12, 15, 18, 21, and 24 times the rms noise of the map, 0.67 mJy beam^{-1}. The synthesized beam, shown in the bottom right corner, is $5\farcs8 \times 5\farcs6$, at P.A. = $-6\fdg4$. White contours correspond to the centimeter emission at 3.6 cm, and trace the UCH II region (Beuther et al. 2004a). Contours are −3, 3, 6, and 9 times 70 μJy beam^{-1}. Grey scale: Continuum image at 2.12 μm from Kumar et al. (2002). Main clumps of dust emission are labeled as BIMA 1 to BIMA 4. White dots indicate the compact millimeter sources detected by Beuther et al. (2004b) at 2.6 mm with the PdBI. These are, from west to east, mm2, mm3, and mm1. White crosses mark the sources from 2MASS with infrared excess, and black tilted crosses mark the position of the Northern Warm Spot (NWS) and the Southern Warm Spot (SWS).

in the same northeast-southwest direction as BIMA 1. Besides this strong component, a weak subcomponent was resolved in the direction of the elongation (to the southwest of mm1), and was labeled mm1a. Beuther et al. (2004b) also find two compact millimeter sources associated with BIMA 2, mm2 and mm3 (see Fig. 1 for the positions of these compact millimeter sources).

In Table 2 we show the position, peak intensity, flux density and masses associated with BIMA 1, BIMA 2, the entire dust ridge (including BIMA 2), BIMA 3, BIMA 4, and IRS 2. We discuss these results in section 4.1.

3.2. CH_3OH

Figure 2a shows the zero-order moment map of the CH_3OH emission, integrated from −1.5 to 21 km s^{-1}, including the two strongest transitions 2_0–1_0 A$^+$, and 2_{-1}–1_{-1} E. Figure 3 shows the CH_3OH spectrum at selected positions. The channel maps corresponding to the lines 2_0–1_0 A$^+$ and 2_{-1}–1_{-1} E are shown in Fig. 4.

The strongest emission of CH_3OH is found to the southeast of BIMA 1, elongated in the southeast-northwest direction, and covering a spatial extension of ∼55″ (0.6 pc). The emission has a fork-like structure (this is well observed in the 7.7 km s^{-1} velocity channel of Fig. 4), and extends through several channels. This structure is associated with high-velocity SiO (2–1) and CO (2–1) emission of outflow B (Beuther et al. 2004a). The position-velocity (p-v) plot along outflow B is shown in Fig. 5a. The most prominent feature in the plot is a blue wing, ∼6 km s^{-1} wide, spanning from 0″ to 15″ offset positions. At negative offsets the CH_3OH emission is dominated by a weak red wing (this is better seen for the 2_{-1}–1_{-1} E line). Farther away than ∼25″ (which corresponds to the southeasternmost clump of outflow B), the emission has contributions from both redshifted and blueshifted emission. This change of behaviour spatially coincides with BIMA 4, located in the p-v plot at an offset position of 20″.

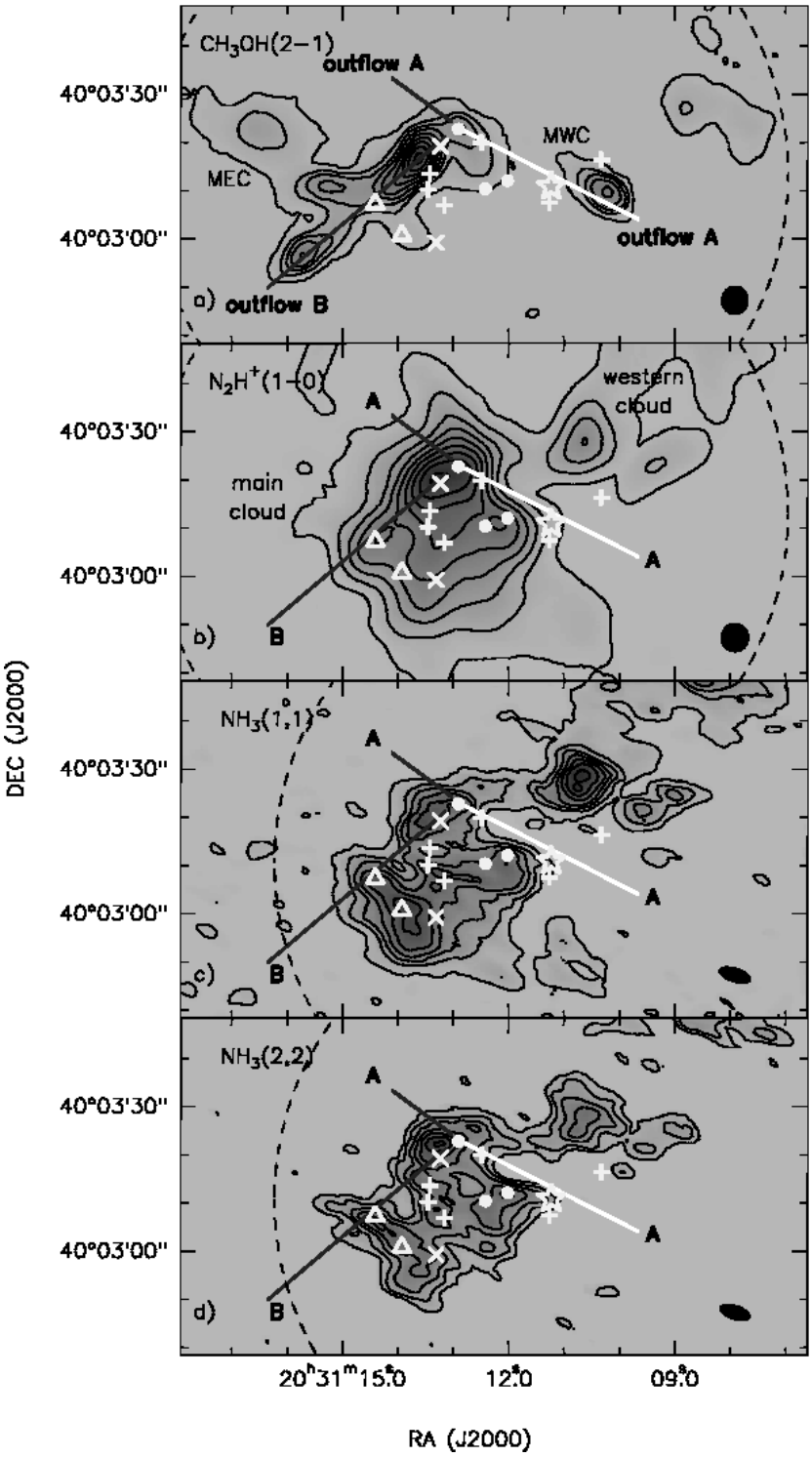

Fig. 2. **a)** CH_3OH zero-order moment for the $2_0–1_0$ A^+, and $2_{-1}–1_{-1}$ E lines toward IRAS 20293+3952. Contours start at 1%, increasing in steps of 12% of the peak intensity, 10.7 Jy beam^{-1} km s^{-1}. **b)** N_2H^+ zero-order moment integrated for all the hyperfine components of the (1–0) transition. Contours start at 2%, increasing in steps of 12% of the peak intensity, 21.9 Jy beam^{-1} km s^{-1}. **c)** NH_3 (1,1) zero-order moment. Contours start at 5%, increasing in steps of 15% of the peak intensity, 0.240 Jy beam^{-1} km s^{-1}. **d)** NH_3 (2,2) zero-order moment. Contours start at 7%, increasing in steps of 15% of the peak intensity, 0.0892 Jy beam^{-1} km s^{-1}. In all panels, the first level is about 3 times the rms noise of the map. Symbols are the same as in Fig. 1, with the star marking the peak of the centimeter emission, and the triangles marking the positions of BIMA 3 and BIMA 4 cores. MEC and MWC stand for methanol eastern clump and methanol western clump, respectively. The synthesized beams for each transition are shown in the bottom right corner, and are listed in Table 1. The straight lines mark the direction of outflows A and B (Beuther et al. 2004a), with the light grey line corresponding to the redshifted lobe. The dashed curve indicates the primary beam of BIMA (panels a and b) and VLA (panels c and d) observations.

Table 2. Parameters of the continuum sources at 3.15 mm

	Peak Position		$I_\nu^{\rm peak}$	Flux[a]	Assumed $T_{\rm d}$[b]	Mass[c]
	α(J2000)	δ(J2000)	(mJy beam^{-1})	(mJy)	(K)	($M_\odot$)
BIMA 1	20:31:12.767	40:03:22.65	17.4	28	34	6.3
BIMA 2	20:31:12.062	40:03:12.22	12.1	23	34	5.2
BIMA 2+ridge	-	-	-	42	25	14
BIMA 3	20:31:13.769	40:03:03.12	5.4	7.9	17	3.9
BIMA 4	20:31:14.558	40:03:06.95	4.2	7.9	17	3.9
IRS 2	20:31:10.303	40:03:17.10	3.5	3.9	50	0.60

[a] Flux density inside the 5σ contour level for BIMA 1, BIMA 2, and BIMA 2+ridge, and the 3σ level for BIMA 3, BIMA 4, and IRS 2.
[b] $T_{\rm d}$ is estimated by correcting the rotational temperature derived from NH_3 (see § 4.2) to kinetic temperature, following the expression of Tafalla et al. (2004). For IRS 2 we assumed $T_{\rm d} \sim 50$ K.
[c] Masses of gas and dust derived assuming a dust emissivity index $\beta = 1$ (Beuther et al. 2004b). The uncertainty in the masses due to the opacity law and the dust emissivity index is estimated to be a factor of four.

A clump to the east of outflow B that can be seen in the integrated intensity map shows narrow lines and appears only at systemic velocities (see Figs. 3 and 4). We label this clump, which has not been previously detected, 'methanol eastern clump'.

In addition, there are two redshifted clumps, one associated with BIMA 1, and the other close to the UCH II region (see, e. g., velocity channels from 13 to 16 km s^{-1}), which probably are part of the redshifted CO (2–1) lobe of outflow A (Beuther et al. 2004a). We label the clump close to the UCH II region 'methanol western clump'. In Fig. 6, showing the p-v plot along outflow A, we find that there is a velocity gradient, from 4 km s^{-1} at 7″, to 8 km s^{-1} at −10″, clearly seen in the two lines. This velocity gradient is centered around the zero offset position (corresponding to mm1). The methanol western clump, seen at ∼ −35″, is highly redshifted (line 2_0–1_0 A$^+$ is at ∼9 km s^{-1}) and shows broad red wings, spreading ∼5 km s^{-1}.

3.3. N_2H^+

The zero-order moment map integrated for all the hyperfine transitions is presented in Fig. 2b. Figure 3 shows the N_2H^+ (1–0) spectra at selected positions.

The integrated N_2H^+ emission consists of a main cloud and a smaller and weaker cloud to the west of the main cloud (western cloud). The size of the main cloud and the western cloud are ∼50″ (0.5 pc), and ∼15″ (0.15 pc), respectively. The four BIMA sources are located in the main cloud with BIMA 1 close to the N_2H^+ emission peak. N_2H^+ emission is marginally detected towards the UCH II region.

The hyperfine $F_1 = 0$–1 was used for the analysis of the kinematics of the N_2H^+ emission because it is not blended with the other hyperfines. In Figs. 7 and 8 we show the channel maps and the first and second-order moments for this hyperfine. The channel with maximum intensity was found at the systemic velocity (6.3 km s^{-1}).

The first-order moment map shows a small velocity gradient in the main cloud with increasing velocities roughly from the southwest to the northeast. In addition, there is a filament spatially coincident with outflow B (clearly visible in the 7.1 to 7.7 km s^{-1} channel maps of Fig. 7), which has very broad lines associated, as seen in the second-order moment map (Fig. 8b). The p-v plot made across outflow B and within the main cloud (Fig. 5b) shows the aforementioned velocity gradient in the main cloud and the line broadening toward outflow B (at offset position zero). The p-v plot along outflow B (Fig. 5c) shows clear line broadening all along the outflow, but without the wing emission component found in the CH_3OH emission.

The western cloud appears redshifted, at ≥ 7 km s^{-1}, and has narrow lines (Fig. 7). At these velocities, there is weak emission connecting the western cloud with outflow B. Figure 9 shows the p-v plot along a cut at P.A.=110°, picking up partially the outflow and the western cloud. From this plot, it seems that the western cloud extends ∼1′ (0.6 pc) toward the east, intersecting the main cloud.

3.4. NH_3

The zero-order moment map of the NH_3 (1,1) emission (integrated including the main line and the inner satellites) is shown in Fig. 2c. The overall structure of NH_3 (1,1) resembles roughly the emission of the dust and the emission of N_2H^+. NH_3 (1,1) emission is also associated with the main cloud and the western cloud. There is another NH_3 (1,1) clump to the northwest (not shown in Fig. 2), which is very weak in N_2H^+ (in part due to the primary beam attenuation). A difference between N_2H^+ and NH_3 (1,1) emission is that whereas N_2H^+ peaks close to the millimeter continuum sources, the strongest NH_3 (1,1) emission in the main cloud lies in the southeastern part. In addition, the strongest NH_3 (1,1) emission over the entire region comes from the western cloud, not from the main cloud. NH_3 (1,1) emission toward the UCH II region is weak.

Figure 2d shows the zero-order moment map of the NH_3 (2,2) emission. NH_3 (2,2) emission resembles closely that of the NH_3 (1,1). However, the main difference with NH_3 (1,1) is that the strongest emission of the NH_3 (2,2) in the entire region is found very close to BIMA 1. The NH_3 (2,2) emission in the western edge of the main cloud shows an extension that encompasses the position of the UCH II region.

Note that the dense gas traced by NH_3 and N_2H^+ is morphologically very different from the gas traced by CH_3OH.

4. Analysis

4.1. Dust

We compared the position of BIMA 1 with the millimeter source found by Beuther et al. (2004b) at 3.5 mm at similar angular resolution. The peak of BIMA 1 is shifted ∼1″ to the west of mm1. The values of the peak intensities (Table 2) are in very good agreement with Beuther et al. (2004a), and the flux densities from Table 2 are about 50% larger than those reported in Beuther et al. (2004a). The offset in positions and the larger flux

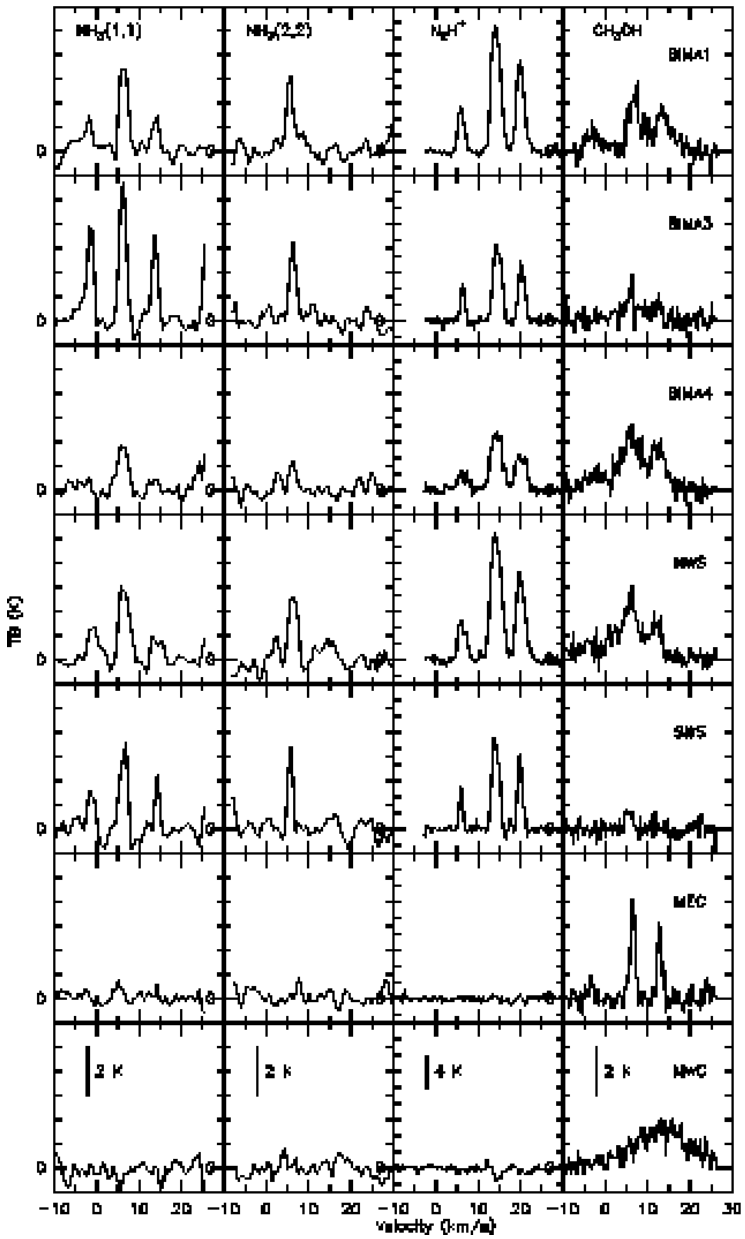

Fig. 3. Spectra toward seven positions of the IRAS 20293+3952 region for the four transitions studied in this paper, from left to right, NH_3 (1,1), NH_3 (2,2), N_2H^+ (1–0), and CH_3OH (2–1). The seven positions are labeled on the right panel of each row, and are, from top to bottom, BIMA 1, BIMA 3, BIMA 4, NWS (Northern Warm Spot), SWS (Southern Warm Spot), MEC (methanol eastern clump), and MWC (methanol western clump). The vertical scale is indicated for each transition in the bottom row. For CH_3OH we show, in order of increasing velocity, the 2_0–1_0 E, 2_0–1_0 A^+, and 2_{-1}–1_{-1} E lines (velocities are referred to the 2_0–1_0 A^+ line). For N_2H^+, velocities are referred to the $F_1 = 0$–1 hyperfine.

densities detected in this work could be produced by the different spatial filtering of the BIMA and PdBI arrays, with the BIMA array more sensitive to large-scale structures.

The continuum emission at 3.15 mm is probably due to thermal dust emission for most positions of the region, since free-free emission from ionized gas, traced by the continuum emission at 3.6 cm (Fig. 1), is detected only at the western edge of the main cloud, at the position of the UCH II region. However, Beuther et al. (2004b) find a spectral index between 1.3 and 2.6 mm toward mm1a (the subcomponent to the west of mm1) of 0.8, and suggest that the collimated ionized wind from outflow A could account for such a spectral index. The contribution of the possible free-free emission from mm1a to BIMA 1 is small, given that the intensity of mm1 is five times larger than the intensity of mm1a, and thus essentially all continuum emission at 3 mm is due to thermal dust emission.

To derive masses from the flux densities at 3.15 mm, we corrected the rotational temperature, between 15 and 25 K (calculated from NH_3 (1,1) and NH_3 (2,2), see § 4.2), to kinetic temperature (Walmsley & Ungerechts 1983), by following Tafalla et al. (2004), yielding kinetic temperatures in the range 17–34 K. The masses (Table 2) are 2 times larger than those obtained by Beuther et al. (2004b) from observations at 3.5 mm. The difference arises from the fact that BIMA is detecting more flux than

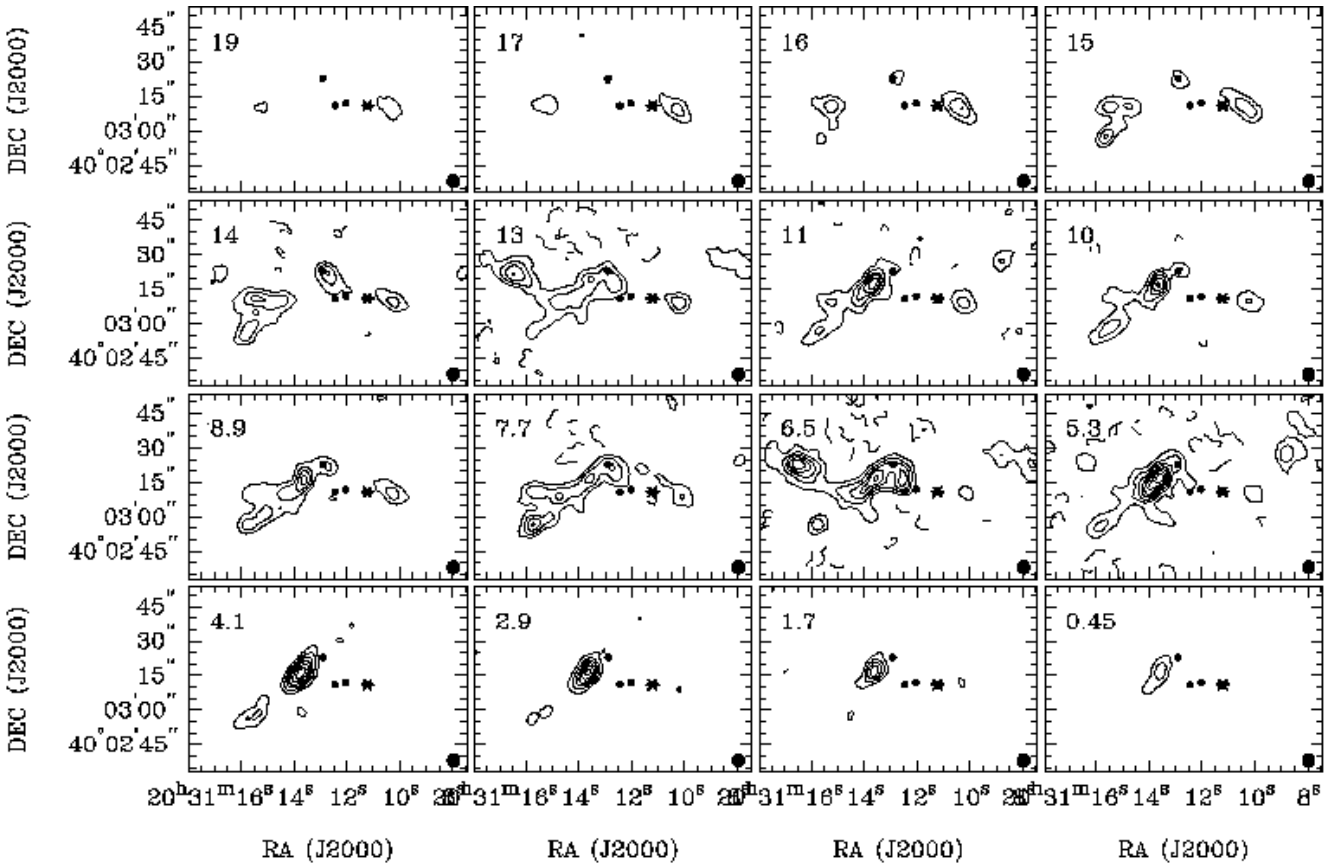

Fig. 4. CH_3OH channel maps toward IRAS 20293+3952 for the lines 2_0–1_0 A^+ (around 6.3 km s^{-1}, the systemic velocity), and 2_{-1}–1_{-1} E (around 13 km s^{-1}), averaged every 4 channels. Contours are −16, −12, −8, −4, 4, 8, 12, 16, 20, 24, 28, and 32 times the rms of the map, 0.04 Jy $beam^{-1}$. Filled circles are the compact millimeter sources detected by Beuther et al. (2004b), and the star marks the position of the UCH II region. The synthesized beam is shown in the bottom right corner of each panel.

PdBI observations, and from the different dust temperatures assumed. While Beuther et al. (2004a) assume a dust temperature (derived from a graybody fit to the spectral energy distribution in the entire region) of 56 K, we adopted the kinetic temperatures obtained from the NH_3 observations, which allowed us to separate the contribution from each source, thanks to the high angular resolution. The lower temperatures adopted imply larger masses in order to produce the same flux density.

4.2. Rotational temperature and column density maps

We obtained N_2H^+ and NH_3 spectra for positions in a grid of $2'' \times 2''$ in the main cloud and the western cloud, and fitted the hyperfine structure of each spectrum, or a single Gaussian for NH_3 (2,2). We performed the fits only for those spectra with an intensity greater than 5σ for NH_3 (1,1), and greater than 4σ for NH_3 (2,2). We set a higher cutoff for NH_3 (1,1) to ensure that not only the main line is detected but also the satellites. The results from the fits indicate that the entire main cloud is essentially optically thin for N_2H^+ ($\tau_{\rm TOT} \leq 1.5$), but optically thick for NH_3 (1,1) ($\tau_{\rm TOT} \leq 12$). In both cases, the highest opacities are reached in the southeastern side of the cloud, around BIMA 3.

From the results of the fits to the NH_3 (1,1) and the NH_3 (2,2) spectra we computed the rotational temperature and NH_3 column density maps. We derived the rotational temperature following the standard procedures (Ho & Townes 1983; Sepúlveda 1993), and assuming that the excitation temperature and the intrinsic line width were the same for both NH_3 (1,1) and NH_3 (2,2). For the NH_3 column density derivation, we followed the expression given in Table 1 of Anglada et al. (1995), and assumed that the filling factor was 1.

The map of the rotational temperature is presented in Fig. 10a. The maximum value, 38 ± 15 K, is reached at the position of the UCH II region. Interestingly, around the apparent dense gas cavity west to BIMA 1, NH_3 shows high temperatures, with a maximum of 34 ± 9 K (the fits to the NH_3 (1,1) and NH_3 (2,2) at these positions are reasonably good, so this heating must be real). Toward the western cloud we find that temperature is essentially constant, around 16 K, slightly decreasing toward the center of the cloud.

There are some local maxima of rotational temperature in the map. In order to test the significance of these local maxima, we fitted them with a 'gaussian + background level' model in a region a few times the synthesized beam size, with the gaussian width and position angle fixed and equal to the synthesized beam. We defined the temperature enhancement as the difference between the local maxima and the background level. The rms of the residual image in the fitted region is < 1.5 K, and the positions of the gaussian peaks are within 0.″2 of the local maxima positions. In Table 3 we list the positions of the significant local maxima, their temperature, and temperature enhancement. We considered that a local maxima is significant when the temperature enhancement is at least two times the uncertainty. There is a local maximum that is nearly coincident (within 0.″5) with

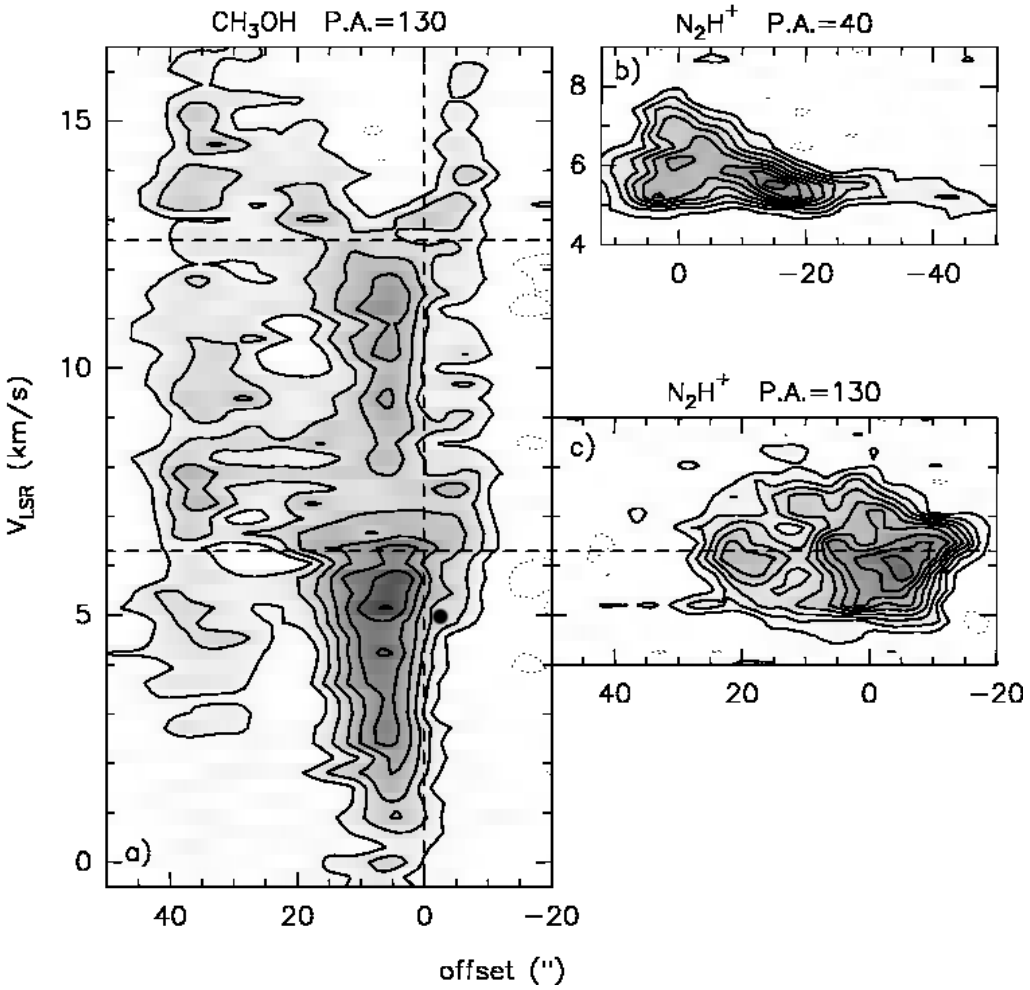

Fig. 5. a) CH_3OH position-velocity (p-v) plot along outflow B (P.A.=130°). Channel maps have been convolved with a beam of $5'' \times 2''$, with P.A. perpendicular to the direction of the cut. Contours start at 0.17 Jy beam^{-1}, and increase in steps of 0.17 Jy beam^{-1}. The bottom dashed line indicates the systemic velocity for line 2_0–1_0 A$^+$ (taken as the reference line), at 6.3 km s^{-1}. The top dashed line indicates the systemic velocity for line 2_{-1}–1_{-1} E, at 12.6 km s^{-1}. **b)** N_2H^+ p-v plot for the F_1 = 0–1 hyperfine across outflow B and the main cloud (P.A.=40°). Positive positions are toward the northeast. Contours start at 0.2 Jy beam^{-1}, increasing in steps of 0.2 Jy beam^{-1}. **c)** N_2H^+ p-v plot for the F_1 = 0–1 hyperfine along outflow B (P.A.=130°). The velocity scale is placed matching the velocity scale of the CH_3OH emission. Contours start at 0.15 Jy beam^{-1}, increasing in steps of 0.15 Jy beam^{-1}. For N_2H^+, we did not convolve the channel maps. In all panels, the central position corresponds to the Northern Warm Spot (see Table 4), and is marked by a vertical dashed line in panel a.

IRS 5, with a value of 24 ± 3 K. The warmest local maximum is located ∼5″ to the southeast of mm1 (labeled as 'Northern Warm Spot'), reaching 29 ± 6 K, and is apparently associated with faint continuum emission at 2.12 μm (see Fig. 1). There is another local maximum associated also with faint emission at 2.12 μm, which is found 10″ to the southwest of BIMA 3, with 20 ± 2 K (labeled as 'Southern Warm Spot'). Another local maximum is associated with the H_2 knot c (Kumar et al. 2002), lying on the axis of outflow B. Finally, note that there is also some heating about 20″ to the southeast of the Northern Warm Spot, but we did not consider this heating in the table because it falls in the edge of the region where we fitted the spectra. Note that all the temperature enhancements in Table 3 have infrared emission associated, giving support to their significance.

Figure 10b shows the resulting column density map for NH_3, corrected for the primary beam response. An obvious feature from the NH_3 column density map is that the highest values are found to the southeast of the main cloud, where we found the lowest values in the rotational temperature map (Fig. 10a). In the northern part of the cloud the column density is higher around the Northern Warm Spot. It is worth noting that the NH_3 column density decreases toward IRS 5. Note also that in the western cloud the column density increases toward the center.

We calculated the N_2H^+ column density by following Benson et al. (1998), taking into account the opacity effects, and correcting for the primary beam attenuation. In the expression for the column density, the value for T_{ex} was derived from the hyperfine fit made with CLASS, and assuming a filling factor of 1. The resulting map is shown in Fig. 10c. Contrary to NH_3, the map of the N_2H^+ column density has the maximum value very close to the position of the Northern Warm Spot and BIMA 1, and not in the southern side of the main cloud.

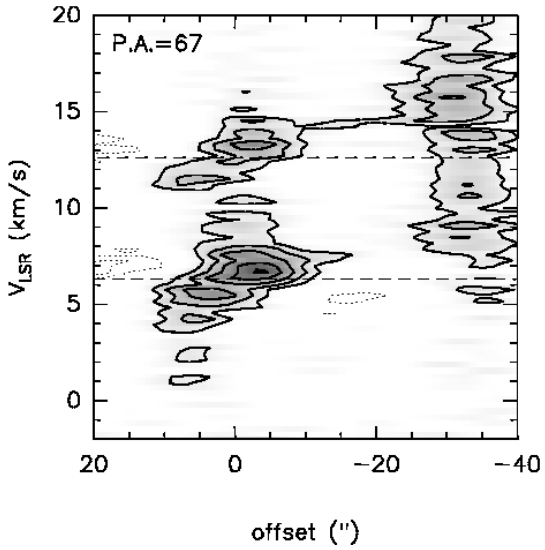

Fig. 6. CH_3OH p-v plot along outflow A, with P.A.=67°. Contours are −0.25, −0.15, 0.15, 0.25, 0.35, 0.45, and 0.52 Jy beam^{-1}. The velocity resolution is 0.30 km s^{-1}, and the channel maps have been convolved with a beam of 10″ × 5″, with a P.A. perpendicular to the direction of the cut, in order to recover the maximum emission in each position. The velocity range includes two lines: 2_0–1_0 A^+ (at 6.3 km s^{-1}, bottom dashed line) and 2_{-1}–1_{-1} E (at 12.6 km s^{-1}, top dashed line). The zero position corresponds to mm1, and positive values go to the northeast.

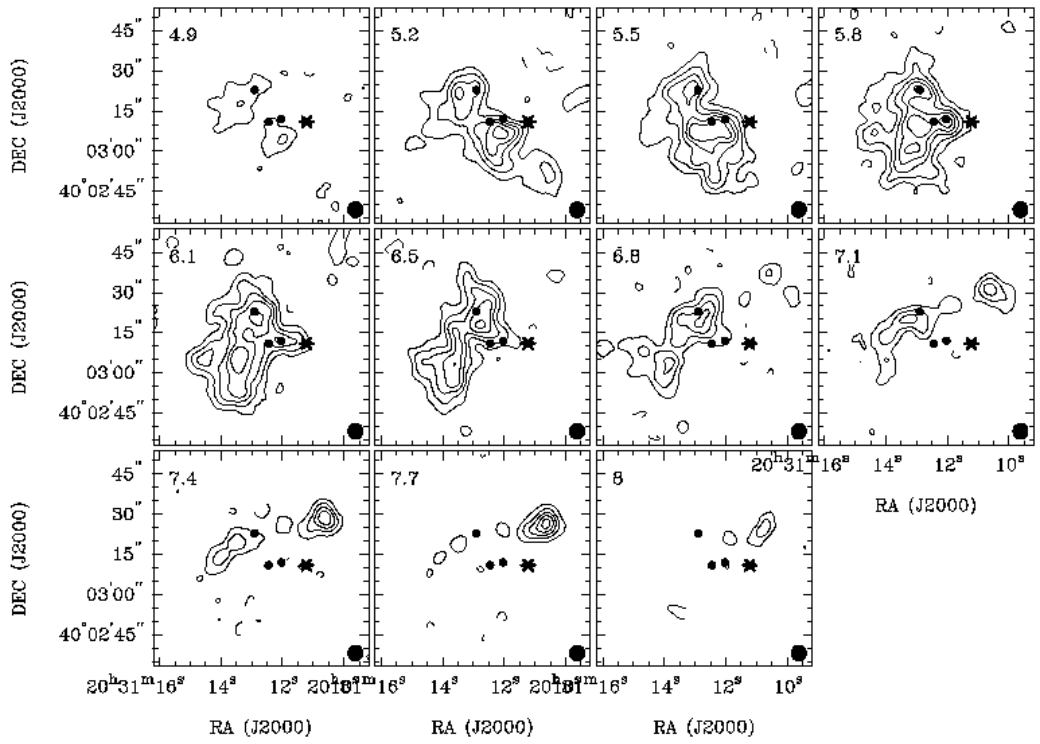

Fig. 7. N_2H^+ (1–0) channel maps for the F_1 = 0–1 hyperfine toward IRAS 20293+3952. Contour levels are −4, 4, 8, 12, 16, and 20 times the rms noise of the maps 0.07 Jy beam^{-1}. Filled circles are the compact millimeter sources detected by Beuther et al. (2004b), and the star marks the position of the UCH II region. The synthesized beam is shown in the bottom right corner.

4.3. The NH_3/N_2H^+ column density ratio map

In order to compare the NH_3 emission with the N_2H^+ emission, we convolved the NH_3 and N_2H^+ channel maps to obtain a final beam of 7″ (the major axis of the NH_3 and N_2H^+ beams). We fitted the spectra in each position of a grid of 4″ × 4″ in the convolved maps, and derived the column density for NH_3 and N_2H^+ following the same procedures outlined above, and correcting for the primary beam of each interferometer. We computed the NH_3/N_2H^+ column density ratio map, and the result is shown in Fig. 10d. From the NH_3/N_2H^+ ratio map, one can see a clear gradient from the northwest of the main cloud, with a ratio around

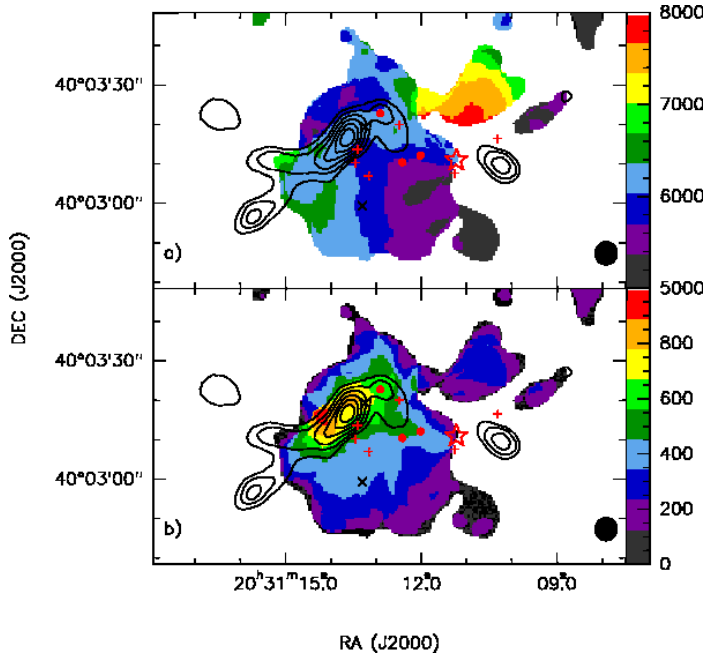

Fig. 8. a) Color scale: first-order moment map for the hyperfine $F_1 = 0–1$ line of N_2H^+ (1–0) toward IRAS 20293+3952. **b)** Color scale: second-order moment map for the hyperfine $F_1 = 0–1$ line of N_2H^+ (1–0). In both figures black contours are the same as Fig. 2a, showing the CH_3OH (2–1) emission, with contours starting at 13%, and increasing in steps of 15% of the peak intensity. Color scales are in m s^{-1}. The synthesized beam is shown in the bottom right corner, and symbols are the same as in Fig. 2. Note that the second-order moment gives the velocity dispersion, and must be multiplied by the factor $2\sqrt{2\ln 2} \simeq 2.35$ to obtain FWHM line widths.

Table 3. Significant local temperature enhancements

Position		T_{rot}	ΔT[a]	Possible
α(J2000)	δ(J2000)	(K)	(K)	Counterparts
20:31:13.26	40:02:58.9	20 ± 2	7 ± 2	2.12 μm faint emission (SWS[b])
20:31:13.23	40:03:19.5	29 ± 6	12 ± 6	2.12 μm faint emission (NWS[b])
20:31:13.44	40:03:13.4	24 ± 3	7 ± 3	IRS 5
20:31:14.96	40:03:03.4	23 ± 4	9 ± 4	H_2 knot c [c]

[a] We assumed that each local maximum can be described by a 'gaussian + background level' model, with the gaussian width and position angle fixed and equal to the synthesized beam. The temperature enhancement, ΔT, is defined as the difference between the local maximum and the background level. We considered as significant the temperature enhancements with $\Delta T \geq 2\sigma$, with σ being the uncertainty.
[b] NWS: Northern Warm Spot; SWS: Southern Warm Spot
[c] from Kumar et al. (2002).

50, to the southeast, where the ratio reaches values up to ~300. Such high values are also reached in the western cloud.

5. Discussion

5.1. General properties of the dense gas

5.1.1. Rotational temperature

The temperature distribution in the main cloud can be clearly separated into two parts: the northern side, with an average temperature of ~22 K, and the southern side, with an average temperature of ~16 K. It is interesting to note that almost all the YSOs in the region (§ 5.3) are associated with the northern side of the cloud, while in the cold southern side we found very few hints of active star formation. Thus, the higher temperature in the northern side is probably due to internal heating from the embedded YSOs. As for the southern side, the average temperature of 16 K is higher than typical temperatures for low-mass externally heated starless cores (~10 K, e. g., Tafalla et al. 2002, 2004). Such higher temperatures could indicate that there are low-mass non-detected YSOs heating the southern side of the main cloud, or that there is external heating. A similar result was found by Li et al. (2003), who derived temperatures of ~15 K toward massive (with masses similar to the mass derived for the main cloud, see next paragraph) quiescent cores, with no signs of star formation, in Orion. Li et al. (2003) find that the temperatures of the massive quiescent cores can be well explained by the dust being heated by the external UV field from the Trapezium, at a distance of ~1 pc from the massive cores. In our case, the B1 star associated with the UCH II region (see § 5.3) could be the source of heating of the southern side of the main cloud, at ~0.5 pc from the UCH II region. However, we find no temperaure gradient across the south of the main cloud. Alternatively,

the heating could be produced by the nearby O and B stars of the Cygnus OB2 association (Le Duigou & Knödlseder 2002).

5.1.2. Column density and mass

The total mass of gas and dust derived from the dust continuum emission at 3.15 mm, integrated in a region including all the BIMA sources, is ∼100 $M_\odot$ (assuming T_d = 25 K, and β = 1.5), about half of the total mass from dust at 1.2 mm observed with the IRAM 30 m by Beuther et al. (2002a, 2005a), 230 $M_\odot$. We compared this mass with the mass derived from the high-density tracers. The average NH_3 column density for the main cloud, 1.45×10^{15} cm^{-2}, is similar to the values obtained by Jijina et al. (1999) for starless regions, and the derived average N_2H^+ column density of 1.21×10^{13} cm^{-2} agrees with the N_2H^+ column densities obtained by Pirogov et al. (2003) for molecular cloud cores with massive stars and star clusters. The mass estimated for the main cloud from NH_3 is ∼340 $M_\odot$, assuming an abundance for NH_3 of 10^{-8}, and the mass derived from the N_2H^+ column density map is 75–190 $M_\odot$ for N_2H^+ abundances in the range $(2–5)\times10^{-10}$ (Pirogov et al. 2003; Tafalla et al. 2004). Thus, although the uncertainty in the abundances is certainly affecting the estimation of the mass from NH_3 and N_2H^+ (indeed, there is strong chemical differentiation across the main cloud, see § 4.3), we obtained similar masses from the dense gas tracers and the dust emission. Regarding the western cloud, the derived mass from NH_3 and N_2H^+ lies in the range 11–47 $M_\odot$.

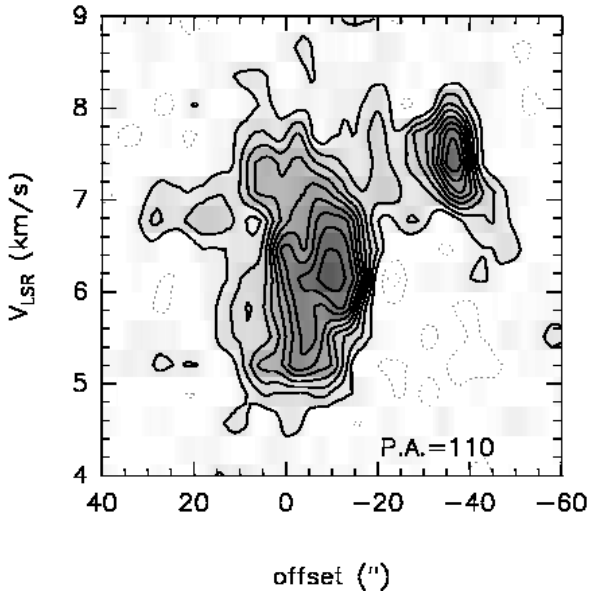

Fig. 9. N_2H^+ p-v plot for the F_1 = 0–1 hyperfine at P.A.=110°, that is, along the western cloud and the northern side of the main cloud. Central position is $\alpha(J2000) = 20^h31^m13^s.63$; $\delta(J2000) = +40°03'16''.7$ (methanol peak), and positive position offsets are toward southeast. Contours start at 0.15 Jy beam^{-1}, increasing in steps of 0.15 Jy beam^{-1}.

5.1.3. Starless core candidates

We identify three starless core candidates in the region: BIMA 3, BIMA 4, and the western cloud. For these three cores, the NH_3 column density is high, $\gtrsim 3\times10^{15}$ cm^{-2}, the rotational temperature is low, ∼14 K, there is no near-infrared emission in the *J*, *H*, and *K* bands of 2MASS, no mid-infrared emission in the 24 μm MIPS (Multiband Imaging Photometer for *Spitzer*[3]) band, and no signs of molecular outflows emanating from the cores (see § 5.2 for a discussion on the outflow emission in BIMA 4). Obviously, these cores could harbor low-mass YSOs (with masses $\lesssim$1 $M_\odot$, as estimated from the available data) non-detected at millimeter and infrared wavelengths. However, the rotational temperature map of Fig. 10a shows local minima associated with these cores, specially with BIMA 4 and the western cloud, supporting that the heating is external and thus that there is no embedded YSO yet.

It is worth noting that, for the three cores, line widths derived from NH_3 (and also N_2H^+) hyperfine fits are around 1 km s^{-1} (Table 4), which are considerably larger than typical line widths measured toward starless cores in low-mass star-forming regions, ∼0.2 km s^{-1} (see, e. g., Crapsi et al. 2005). For the massive quiescent cores studied by Li et al. (2003) the NH_3 line widths were between 0.6 and 0.9 km s^{-1}, similar to what we find. Since the thermal component is around ∼0.2 km s^{-1} at 15 K, the line widths that we found suggest that these cores are dominated by turbulence, as Li et al. (2003) state, or that there are important unresolved ($\lesssim$ 0.05 pc) systematic motions.

5.1.4. Effects of chemical abundance and density

The NH_3/N_2H^+ ratio map of Fig. 10d shows a clear gradient in the ratio across the cloud, from northwest, with low values, to southeast, with the highest values. In particular, there seems to be an anticorrelation between the NH_3/N_2H^+ ratio and the evolutionary stage of the sources embedded in the cloud. On one hand, in the north of the main cloud we found most of the YSOs in the field, where the value of the ratio is < 100. On the other hand, the ratio rises up to ∼300 in the southeastern side of the main cloud and in the western cloud, where we found starless core candidates. The values of the ratio in the entire region are consistent with those derived for low-mass star-forming regions by other authors (Caselli et al. 2002; Hotzel et al. 2004), who also find the same trend of low values (about 60–90) associated with YSOs, and high values (140–190) associated with starless cores.

One could consider whether the high values for the NH_3/N_2H^+ ratio in the southeastern side of the main cloud and in the western cloud are just reflecting the different excitation conditions of NH_3 and N_2H^+, since the critical density of NH_3, $\sim10^4$ cm^{-3} (e. g., Ho 1977), is lower than the critical density of N_2H^+, $\sim10^5$ cm^{-3} (e. g., Joergensen 2004), and thus in regions where the density is $\sim10^4$ cm^{-3}, NH_3 could be thermalized while N_2H^+ is faintly detected because not thermalized. We did a rough estimation of the density in the southeastern side of the main cloud from the continuum emission observed at 3.15 mm toward BIMA 3, adopting the mass derived in this work (see Table 2) and a size of ∼10″, and obtained a volume density of $\sim10^5$ cm^{-3}. For this density, the transitions of both NH_3 and N_2H^+ are thermalized enough to be detectable. Furthermore, as the effects of opacity and different T_{ex} in the cloud were already taken into account in the calculation of the column densities, the different excitation conditions of NH_3 and N_2H^+ cannot play an important role in the large gradient of one order of magnitude in the NH_3/N_2H^+ ratio across the main cloud.

A possible explanation for the higher NH_3/N_2H^+ ratio toward starless cores may be given in terms of abundance and density. For long-lived ($\sim10^6$ yr) cores with moderate densi-

[3] see http://ssc.spitzer.caltech.edu/mips/

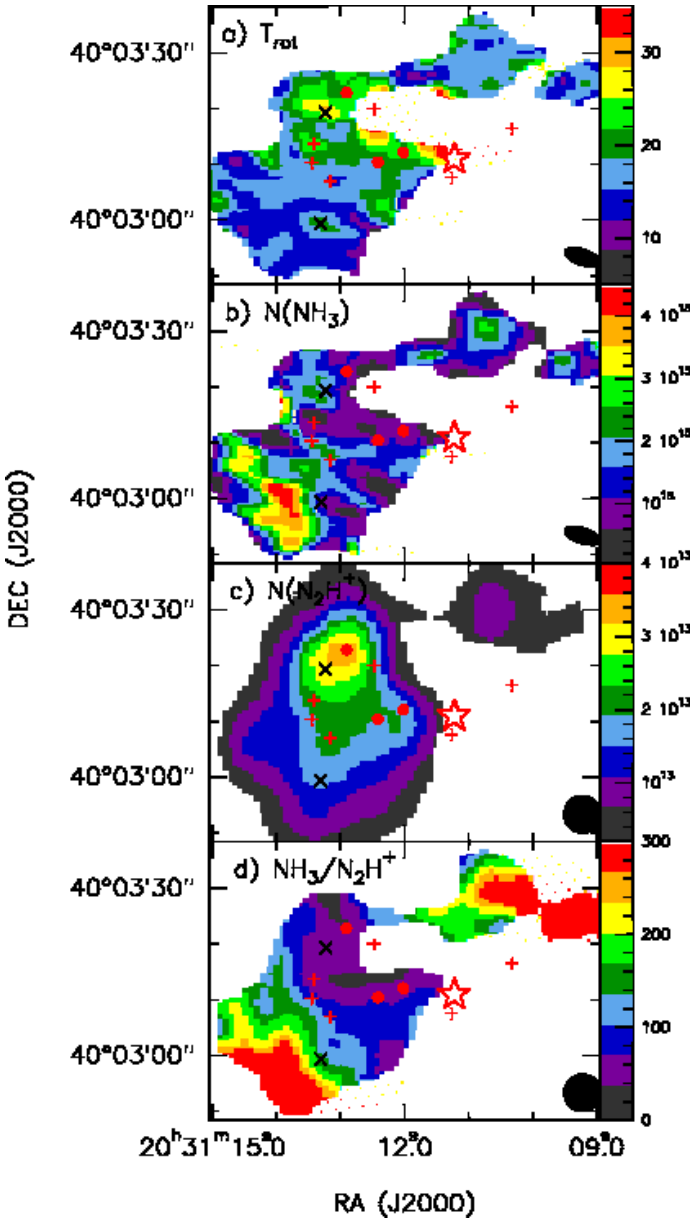

Fig. 10. **a)** Rotational temperature map from NH_3 (1,1) and NH_3 (2,2) obtained for the main cloud and the western cloud of the IRAS 20293+3952 region. Scale units are in K. **b)** NH_3 column density map. Scale units are in cm^{-2}. **c)** N_2H^+ column density map convolved to an angular resolution of 7″. Scale units are in cm^{-2}. **d)** $N(NH_3)/N(N_2H^+)$ ratio map after convolving the NH_3 column density map from panel b to a final angular resolution of 7″. Symbols are the same as in Fig. 2. Beams are shown in the bottom right corner, and are 6.″9 × 3.″0, with P.A.= 71.°5 for panels a and b, and 7″ for panels c and d.

ties (10^4–10^5 cm^{-3}), there is a 'golden period' of high abundance for NH_3 (Aikawa et al. 2005; S. Viti, private communication), while N_2H^+ keeps a constant abundance, as has been seen toward starless cores (e. g., Tafalla et al. 2004). This is consistent with the NH_3/N_2H^+ ratio being high in the southern side of the main cloud, where we find starless cores with faint dust emission, indicating that the volume density is moderate. For higher densities (~10^6 cm^{-3}) one may consider two mechanisms to explain the low NH_3/N_2H^+ ratio. On one hand, the high-density cores, which have short free-fall timescales, may not have enough time to produce an amount of NH_3 comparable to the southern (moderate-density) cores. On the other hand, the NH_3 may start to freeze out onto dust grains, while N_2H^+ seems to remain unaffected up to densities of ~10^7 cm^{-3} (Aikawa et al. 2003, 2005). Note that the temperature in the main cloud is on average low enough so that freezing out of NH_3 is possible (hot spots are very localized). In the main cloud the highest densities are reached in the northern side, where there is the strongest dust emission. We did a rough estimation of the average volume density toward BIMA 1, from the derived mass and the size (at the 5σ contour level) of BIMA 1 (Table 2), and obtained an average volume density toward BIMA 1 of 5×10^5 cm^{-3}. Consequently, we find low values of the ratio associated with high volume densities, and thus, with most of the YSOs in the main cloud.

5.2. Interaction of the YSOs with the surrounding gas

5.2.1. The UCH II region:

In Fig. 11 we overlay the CN (1–0) emission from Beuther et al. (2004b) on the NH_3 (1,1) emission. The morphology of the CN emission next to the UCH II region is following the edge of the dense cloud traced by NH_3 (1,1), and is facing the UCH II region. CN emission is often found in photon-dominated regions, tracing the part of the molecular cloud which is exposed to an intense flux of FUV photons from a nearby young OB star (see, e. g., Fuente et al. 1993; Simon et al. 1997; Boger & Sternberg 2005). In addition, we found heating toward this edge of the cloud (Fig. 10a), with rotational temperature progressively increasing when approaching the UCH II region. All this indicates that the UCH II region is radiatively interacting with the main cloud. The mechanical interaction of the compression front of the UCH II region with the main cloud is likely traced by the H_2 emission at 2.12 μm (Kumar et al. 2002; Beuther et al. 2004a), which reveals a ring-like structure around the UCH II region, of radius ~8″, reaching the edge of the main cloud.

5.2.2. Outflow A:

Beuther et al. (2004a) discovered a highly collimated outflow in CO (2–1) (outflow A), elongated in the northeast-southwest direction, with mm1 being its driving source. The axis of the outflow is shown in Fig. 2.

The velocity gradient seen in CH_3OH toward mm1 (see § 3.2 and Fig. 6) is consistent with tracing material entrained by outflow A. In addition, the p-v plot shows a clump at offset position ~ −35″, the methanol western clump, with wide redshifted wings (see Figs. 3 and 6), and matching well the red lobe of CO (2–1) and the redshifted clump of SiO (2–1) from Beuther et al. (2004b). The methanol western clump appears in the axis of outflow A, just downstream of a weak dust filament that connects IRS 1 and IRS 2 (see Figs. 1 and 2a). This suggests that the interaction of outflow A with the filament sweeps-up and chemically alters the material of the filament, originating the methanol western clump.

The red lobe of outflow A, which starts at mm1, propagates through the cavity apparent in the N_2H^+ and NH_3 zero-order moment maps (see Fig. 2). The rotational temperature and column density maps of Fig. 10 show that the walls of this cavity are characterized by remarkably high temperatures and low column densities. In addition, the NH_3 gas of the walls of the cavity is redshifted (as the lobe of outflow A), and shows line broadening. Thus, this cavity could have been excavated by outflow

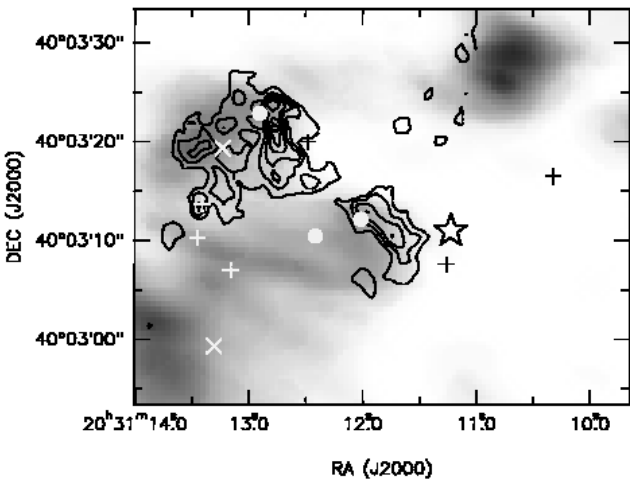

Fig. 11. Zero-order moment map of the CN (1–0) emission (contours) from Beuther et al. (2004b) in the IRAS 20293+3952 region, overlaid on the NH_3 (1,1) emission shown in Fig. 2c (grey scale). CN (1–0) emission has been integrated from 4 to 12 km s^{-1}, and contours start at 15% of the peak intensity, 273 Jy $beam^{-1}$ km s^{-1}, increasing in steps of 15%. Symbols are the same as in Fig. 2. Beams are $6\farcs9 \times 3\farcs0$, with P.A.=72° for NH_3 (1,1), and $1\farcs46 \times 1\farcs21$, with P.A.=32° for CN (1–0).

A, and the high temperatures could arise from the shock interaction of outflow A with the walls of the cavity. This has been observed toward other outflows driven by high-mass stars (e. g., AFGL 5142: Zhang et al. 2002).

5.2.3. Outflow B:

Outflow B was first identified by Beuther et al. (2004a) in SiO (2–1), which shows a very strong blue lobe elongated in the northwest-southeast direction, and in CO (2–1), with faint high-velocity blueshifted emission. CH_3OH emission from outflow B is morphologically very similar to the SiO (2–1) blue lobe and also splits up into two lobes in a fork-like structure at the position of BIMA 4. A scenario in which outflow B is interacting with a starless core, BIMA 4, naturally explains the partial deflection of the outflow seen in the SiO and CH_3OH emission. There are several pieces of evidence that support this scenario. First, the CH_3OH emission splits up and has a change in kinematics when it reaches BIMA 4 (§ 3.2). Second, at this position we found some heating and the NH_3/N_2H^+ abundance ratio shows lower values than those in the southern part of BIMA 4 (Fig. 10a,d; temperature enhancement and chemical variations are signatures of shocked molecular gas, e. g., L1157: Bachiller & Pérez Gutiérrez 1997). Third, the N_2H^+ line broadening along outflow B (which is also observed in NH_3) indicates that the outflow is already interacting with the molecular cloud (Fig. 8b). Finally, downstream of BIMA 4, there is heating (see Fig. 10a) associated with the H_2 knot c of Kumar et al. (2002). The partial deflection of an outflow due to the interaction with a dense quiescent clump has been found toward other star-forming regions (e. g., IRAS 21391+5802, Beltrán et al. 2002). Interaction of an outflow with a dense flattened NH_3 core has been reported too toward NGC 2024 by Ho et al. (1993), where the outflow sweeps the material off the surface of the NH_3 core. Similarly, outflow B interacting with the BIMA 4 core could be also sweeping the material off the surface of the core, producing all the observational features described above.

In addition, the properties of the methanol eastern clump (located 25″ to the northeast of BIMA 4), which is found at ambient velocities, and with narrow lines (around 1 km s^{-1}, Fig. 3), could be a consequence of the illumination by the UV radiation coming from the interaction of outflow B with BIMA 4. The illumination of the UV radiation from shocks has been proposed as the mechanism of enhancement of the emission of some species in clumps ahead of shocks, in particular of CH_3OH and NH_3 (see e. g., Torrelles et al. 1992b; Girart et al. 1994, 2002). With the present observations, we were not very sensitive to the NH_3 emission toward the methanol eastern clump because the clump is located beyond the VLA primary beam FWHM (see Fig. 2c,d). Typically, such illuminated clumps in low-mass star-forming regions have sizes of 0.05–0.1 pc, and are located at distances to the shock of the order of 0.1 pc (Girart et al. 1998). This is consistent with the methanol eastern clump, which has a size of ∼0.15 pc, and is located about 0.2 pc from BIMA 4.

It is interesting to note that the morphological features of the dense gas around outflow B are different from outflow A. While outflow A has already cleared up the dense molecular gas, creating a well defined cavity, outflow B is probably in the embrionary phase of creating the cavity. This suggests that possibly outflow B is younger or less energetic than outflow A, in agreement with the measurements of Beuhter et al. (2004a). It is worth noting that the line width of the dense gas associated with outflow B is significantly higher than the thermal line width for both NH_3 and N_2H^+ (∼ 1.8 km s^{-1} compared to 0.2 km s^{-1}). A similar result is found by Wang et al. (2006) toward massive protostellar cores mapped in NH_3 with high angular resolution. Given that we do not observe systematic motions in the dense gas associated with outflow B, we suggest that the large line width in the dense gas is due to turbulence injected by the passage of the outflow (see Fig. 8b).

Regarding the driving source of outflow B, a possible candidate is mm1, as Beuther et al. (2004b) proposed. If this was the case, mm1 would be a binary system of jet sources, since outflow A is clearly associated with mm1. Another possibility would be that BIMA 4 is the driving source of outflow B. However, the kinematics of the gas as traced by CH_3OH show that there is no clear symmetry with respect to BIMA 4 (see Fig. 5a: BIMA 4 is at an offset position ∼20″). Another candidate of being the driving source of outflow B is the Northern Warm Spot, which is aligned with outflow B, and is located at the begining of the blue lobe of CH_3OH. Furthermore, we found a clear symmetry with respect to the Northern Warm Spot in the p-v plot of Fig. 5a (see § 3.2), strongly suggesting that the Northern Warm Spot could be the driving source of outflow B. In § 5.3 we estimate an associated mass of ∼0.7 $M_\odot$ for the Northern Warm Spot.

Finally, the interaction of outflow B with the BIMA 4 core leads us to speculate that outflow B could be triggering the collapse in this core, as has been proposed in other regions (e. g., Yokogawa et al. 2003). This would draw a scenario in which a YSO in the north of the main cloud is 'responsible' for star formation in the south, but should be further investigated by studying in more detail the morphology and kinematics in the core.

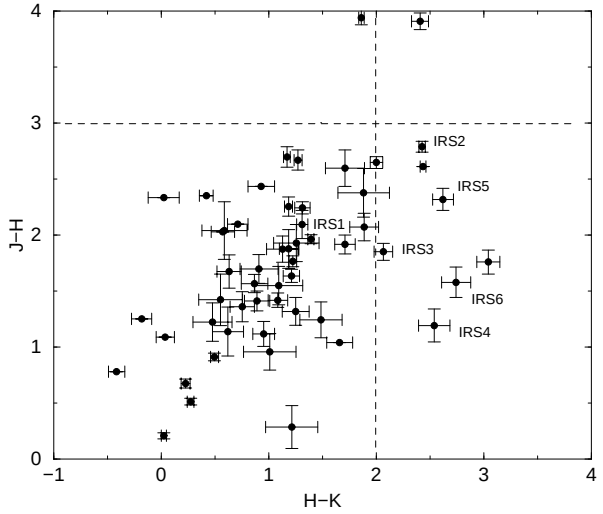

Fig. 12. $(J-H)$, $(H-K)$ diagram for the 2MASS sources in the IRAS 20293+3952 region lying within the BIMA primary beam. We selected those sources, IRS 2 to IRS 6, with $(H-K) > 2$, $(J-H) < 3$, and spatially coincident with the dense gas emission.

5.3. YSOs in the region

5.3.1. Selection of 2MASS sources associated with the region

In order to study the different sources associated with the dense gas found around the UCH II region, we extracted a sample of stars within the BIMA primary beam from the 2MASS Point Source Catalogue (PSC) (Skrutskie et al. 2006), and plotted a $(J-H)$, $(H-K)$ diagram (Fig. 12). The total amount of infrared sources inside the BIMA primary beam is 43. The color-color diagram shows that there is a bulk of infrared stars at low-to-moderate values of the color indices, which occupy the position of stars with no infrared excess, and a group of stars with high $(H-K)$ and low $(J-H)$ colors. We took the criteria of $(H-K) > 2$, $(J-H) < 3$ and spatial coincidence with emission detected in this work to select those 2MASS sources that are possibly (but not necessarily) associated with the dense gas around the UCH II region. The selected 2MASS sources are labeled as IRS 1, IRS 2 (following the nomenclature of Kumar et al. 2002), and IRS 3 to IRS 6 (increasing RA). These infrared sources (with the exception of those that seem to be background/foreground objects, see below) are listed in Table 4 together with the compact millimeter sources from Beuther et al. (2004b), and the sources found in this work. For each source we show the main properties derived in this work.

5.3.2. Individual YSOs

IRS 1 and the UCH II region: From the 2.12 μm image provided by Kumar et al. (2002), we find that IRS 1 is probably a binary system separated $\sim$3″, the fainter component being associated with the UCH II region. The UCH II region has a flux density of 7.6 mJy beam^{-1} at 3.6 cm (Sridharan et al. 2002; Beuther et al. 2004a), and a deconvolved size of 4.″5 (0.04 pc). This corrresponds to an ionizing flux of $\sim 1.5\times10^{45}$ s^{-1}, typical of stars of spectral type B1 (Panagia 1973). Toward the UCH II region, we found the highest rotational temperature in the main cloud, and very low column densities, as expected for gas after the passage of an ionization front (see, e. g., Dyson & Williams 1997).

IRS 2: About 10″ to the northwest of the UCH II region, there is the second brightest infrared source in the field, IRS 2, which shows much more infrared excess than IRS 1, as already stated by Kumar et al. (2002). We could not determine a temperature and column density from NH_3 toward IRS 2 due to the low S/N of the NH_3 emission, but we detected continuum emission at 3.15 mm, and we estimated an associated mass of 0.6 $M_\odot$. The high near-infrared flux of IRS 2 suggests that this is an intermediate-mass YSO.

IRS 3: IRS 3 is the only infrared source with infrared excess falling inside the 2σ contour level of BIMA 1. The high angular resolution observations of Beuther et al. (2004b) reveal a weak extension of mm1 toward the southwest reaching the position of IRS 3. From our data, the dense gas emission was too weak to derive a temperature and column density toward this source. Thus, IRS 3 shows strong infrared emission and weak millimeter emission, indicating that IRS 3 is likely a YSO which is clearing up the material in its surroundings.

IRS 5: IRS 5 falls inside the 7σ contour level of the dust ridge (see Fig. 1), in its eastern edge. We found heating associated with IRS 5 (§ 4.2 and Table 3), indicating that this source is physically associated with the main cloud. In addition, the NH_3 column density is low (Fig. 10b), and thus IRS 5 could be a protostar in the process of clearing up the surrounding material. Alternatively, the low NH_3 column density could be due to depletion of NH_3 onto dust grains.

mm1: mm1 is likely the main contribution to the emission of BIMA 1, since it is the strongest compact millimeter source in the region, and is the driving source of outflow A, which is highly collimated (Beuther et al. 2004a) and elongated in the same direction as BIMA 1 (Fig. 1). In addition, the infrared emission at 2.12 μm associated with mm1 is faint and arises mainly from shocked gas (see Fig. 2 of Kumar et al. 2002). The rotational temperature toward mm1 is 24 ± 3 K (Table 4), and the NH_3 column density is rather low, possibly due to depletion of NH_3 onto dust grains. From the flux density of Beuther et al. (2004b) at 2.6 mm, we obtain a mass for mm1 of 4.0 $M_\odot$, assuming $\beta = 1$ (value estimated by Beuther et al. 2004b), and $T_{\rm d} = 32$ K (estimated from the rotational temperature derived in this work). All this indicates that mm1, in contrast with IRS 3, is deeply embedded in a massive and not very hot envelope, suggesting that it is an intermediate/high-mass protostar.

mm2 and mm3: Beuther et al. (2004a) detect two compact millimeter sources inside the 5σ contour level of BIMA 2, mm2 and mm3, and they suggest that each one is driving a molecular high-velocity CO (2–1) outflow (outflows C and D), which indicates that mm2 and mm3 are truly protostars, and not heated clumps of dust without any star yet. Taking the flux density from Beuther et al. (2004b) at 2.6 mm, a dust emissivity index $\beta = 1$, and $T_{\rm d} = 30$ K and $T_{\rm d} = 23$ K for mm2 and mm3 respectively ($T_{\rm d}$ derived from this work, as in the case of mm1), we estimate associated masses of 1.3 $M_\odot$ for mm2 and 0.8 $M_\odot$ for mm3.

Table 4. List of sources in the I20293 region

	Position[a]			$\Delta v(NH_3)$ [c]	$N(NH_3)$		T_{rot}	I_ν^{peak} [e]	M_c [f]
	α(J2000)	δ(J2000)	Outf [b]	(km s^{-1})	(10^{15} cm^{-2})	Ratio [d]	(K)	(mJy beam^{-1})	($M_\odot$)
YSOs									
IRS 1	20:31:11.26	+40:03:07.6	NN	-	-	-	-	3.9	0.6
UCH II	20:31:11.22	+40:03:11.0	NN	2.4 ± 0.3	0.14	57	38 ± 15	4.0	0.4
IRS 2	20:31:10.32	+40:03:16.5	NN	-		-	-	3.5	0.5
IRS 3	20:31:12.48	+40:03:20.0	YN	-	-	-	-	9.5	1.4
IRS 5	20:31:13.41	+40:03:13.7	?N	1.53 ± 0.06	0.59	42	24 ± 3	5.2	1.2
mm1	20:31:12.9	+40:03:22.9	YY	1.37 ± 0.12	1.1	37	24 ± 3	28.0[g]	4.0
mm2	20:31:12.01	+40:03:12.2	YN	1.10 ± 0.07	0.88	46	23 ± 4	8.6[g]	1.3
mm3	20:31:12.41	+40:03:10.5	YN	1.23 ± 0.13	0.66	57	19 ± 1	3.6[g]	0.8
NWS[h]	20:31:13.23	+40:03:19.5	NY	2.00 ± 0.11	1.8	56	29 ± 6	3.7	0.7
SWS[h]	20:31:13.26	+40:02:58.9	YN	$\lesssim$1.03±0.04	1.3	150	20 ± 2	< 0.28	< 0.9
Starless Cores									
BIMA 3	20:31:13.92	+40:03:00.9	NN	1.18 ± 0.06	5.4	290	14 ± 2	4.0	2.2
BIMA 4	20:31:14.40	+40:03:07.4	YY	1.34 ± 0.06	3.8	180	14 ± 2	3.5	2.0
WCloud[h]	20:31:10.71	+40:03:30.3	NN	$\lesssim$1.03±0.02	2.8	280	15 ± 3	< 0.28	< 1.3

[a] Positions correspond to those in the 2MASS PSC for IRS 1 to IRS 5; the centimeter source given by Beuther et al. (2002b) for the UCH II region; the positions given by Beuther et al. (2004b) for mm1 to mm3; the peak in the rotational temperature map of Fig.10a for the NWS and the SWS, and the position of the peak in the NH_3 column density map of Fig.10b for the starless cores.
[b] High-velocity outflow associated (Y=Yes; N=No): the first character refers to CO from Beuther et al. (2004a), the second character refers to high-velocity CH_3OH from this work.
[c] Line width derived from the fits to the hyperfine structure of NH_3(1,1) (see § 4.2).
[d] Ratio of $N(NH_3)$ over $N(N_2H^+)$.
[e] Intensities at 3.15 mm from this work. The rms noise is 0.7 mJy beam^{-1}, and the upper limits for non-detections have been set to 4σ.
[f] Associated mass (essentially circumstellar) from the mm continuum emission listed in column (9), assuming a dust emissivity index $\beta = 1$, and estimating the kinetic temperature from the rotational temperature listed in column (8), following the expression of Tafalla et al. (2004, see § 5.3).
[g] For mm1, mm2, and mm3 the intensity corresponds to the flux density (in mJy) given by Beuther et al. (2004b).
[h] NWS: Northern Warm Spot; SWS: Southern Warm Spot; WCloud: western cloud (see Fig. 2b).

The Northern Warm Spot: The Northern Warm Spot is located about 5″ (10000 AU) to the southeast of mm1, and is near a local maximum in NH_3 and N_2H^+ column densities (see Fig. 10b and c). From the millimeter continuum emission we estimated an associated mass of ∼0.7 $M_\odot$ (assuming $\beta = 1$ and $T_d = 44$ K). Very close to the warm spot, 1.″3 to the east, there is faint infrared continuum emission at 2.12 μm, which is not detected in the *J* and *H* band images of 2MASS, indicating that the source has strong infrared excess. Since there is no H_2 line emission at 2.12 μm tracing shocked gas (see Fig. 2 of Kumar et al. 2002), the infrared emission is most likely tracing an embedded protostar, and not a condensation heated up by the impact of outflow B. These properties support that the Northern Warm Spot is the driving source of outflow B.

The Southern Warm Spot: Similar to the NWS, the Southern Warm Spot is found ∼10″ to the southwest of BIMA 3 (see §4.2). At this position, the temperature enhancement is very significant (see Table 3), and we also found faint infrared emission associated, present only in the *K* filter of 2MASS, and with no H_2 line emission associated. The emission from the continuum at 3.15 mm is below 4σ, implying an associated mass $\lesssim$ 0.9 $M_\odot$ (assuming $T_d = 25$ K, estimated as in the case of mm1). Furthermore, there is high-velocity blueshifted CO (2–1) emission spatially coincident with the Southern Warm Spot (Beuther et al. 2004a). All this indicates that possibly the heating in the Southern Warm Spot is due to an embedded low-mass YSO.

Background/foreground objects: In addition to IRS 5, we find two 2MASS sources with infrared excess, IRS 4 and IRS 6, spatially coincident with the dust ridge. IRS 6 is the source with the highest infrared excess among the 2MASS sources in the main cloud, suggesting that it is embedded in gas and dust. The faint source IRS 4 is located only 4″ to the southwest of IRS 6, and also shows infrared excess. However, the association of IRS 4 and IRS 6 with the dense gas is not clear from the rotational temperature and NH_3 column density maps (Fig. 10a,b), and thus these two infrared sources could be highly extincted background stars or foreground YSOs belonging to the cluster.

Summary: As seen above, there is a variety of YSOs in the region. The most massive sources seem to be the UCH II region, IRS 1, and IRS 2. To the east of the massive sources, there is the main cloud of dense gas, where we find seven sources (IRS 3, IRS 5, mm1, mm2, mm3, the Northern Warm Spot and the Southern Warm Spot), which seem to be (proto)stars coming from the same natal cloud. In addition, we found three cores with characteristics similar to starless cores. The sources seem to be in different evolutionary stages, with the infrared sources in the more advanced phases, the millimeter sources with no infrared emission likely being in an earlier stage, and the youngest sources having the properties of starless cores. We do not find different evolutionary stages only between the low-mass sources and the high-mass sources (which are expected because the high-mass sources evolve more rapidly to the main sequence than the low-mass sources), but among the low-mass sources as well, for which we expect similar rates of evolution to the main sequence. For example, IRS 3 and IRS 5 are

YSOs strongly emitting in the infrared but with faint millimeter emission, and do not seem to be driving outflows, suggestive of being at the end of the accretion phase. Contrary to this, mm2 and mm3 are YSOs with the millimeter emission much stronger than the infrared emission, and they are the driving sources of collimated outflows, indicative of being in the main accretion phase. The masses of IRS 3 and IRS 5 are difficult to estimate, but comparing with the infrared emission of the known intermediate/high-mass sources one may classify them as low-mass YSOs. The masses of mm2 and mm3, estimated from the millimeter emission, are around 1 $M_{\odot}$. Thus, these low-mass YSOs (IRS 3/IRS 5, and mm2/mm3) seem to be in different evolutionary stages, and we conclude that stars are not forming simultaneously in this cluster environment. Rather, there may be different generations, as found toward other star-forming regions (e. g., NGC 6334: Beuther et al. 2005b; S235A-B: Felli et al. 2006; L1551: Moriarty-Schieven et al. 2006).

5.4. Spatial distribution of the YSOs in the region

In this section we consider whether interaction between the different sources is important in the determination of the spatial distribution of the YSOs. We find that star formation is localized in the north of the main cloud, where there are around six YSOs, while in the south we find sources with properties of starless cores, and only one YSO.

We consider first whether the UCH II is responsible for such a spatial distribution. In section 5.2 we discussed some evidence of interaction of the UCH II region with the edges of the main cloud, mainly with BIMA 2. This suggests that mm2 and mm3 could have been triggered by the UCH II region. If this was the case, one would expect to find some evidence of a compression front expanding away from the UCH II region. In the p-v plot of Fig. 9, the N_2H^+ emission shows the shape of an incomplete ring, which could be interpreted as an incomplete expanding shell. However, the velocity field as seen from N_2H^+ in Fig. 8b does not show any radial symmetry with respect to the UCH II region, and the presence of outflow B makes difficult to disentangle the advance of any compression front. In addition, the formation of the YSOs in the northeast of the main cloud is not likely due to triggering by the UCH II region, since they are located farther away than mm2 and mm3 and are not in earlier evolutionary stages. Therefore, triggering by the UCH II region does not seem to be the dominant agent causing star formation in this clustered environment.

Another possibility for the formation of the YSOs in the north of the main cloud could be a merging of the main cloud with the western cloud. In Fig. 9, we found that the western cloud has an extension intersecting the main cloud, seen at velocities > 7 km s^{-1} in the channel maps (Fig. 7). Merging of two clouds has been proposed as a mechanism to trigger star formation in other regions, (Wiseman & Ho 1996; Girart et al. 1997; Looney et al. 2006; Peretto et al. 2006). Note however that no further evidence of such a merging (heating, line broadening, two clear velocity components across the main cloud) is seen associated with the extension of the western cloud, and thus the merging scenario is not fully consistent with our data.

We therefore conclude that the spatial distribution of the YSOs in this cluster environment could simply reflect the initial conditions of the cloud: if the main cloud was originally much denser in the north than in the south, we would possibly observe a similar situation to what we have found.

6. Conclusions

We observed with the BIMA and VLA arrays the continuum emission at 3.15 mm, and the N_2H^+, NH_3, and CH_3OH emission toward IRAS 20293+3952, a region in which star formation is taking place in a closely-packed environment. Our main conclusions can be summarized as follows:

1. The dense gas traced by N_2H^+ and NH_3 shows two different clouds, one to the east of the UCH II region (main cloud), of ∼0.5 pc of size and ∼250 $M_{\odot}$, and another cloud to the northwest (western cloud), of ∼0.15 pc and ∼30 $M_{\odot}$, and redshifted with respect to the main cloud. The dust emission reveals two strong components in the northern side of the main cloud, BIMA 1 and BIMA 2, and two fainter components in the southern side, BIMA 3 and BIMA 4, together with extended dust emission forming a common envelope. Regarding the CH_3OH, we found strong emission in a fork-like structure associated with outflow B from Beuther et al. (2004a), as well as two CH_3OH clumps associated with outflow A.
2. We found that the rotational temperature is higher in the northern side of the main cloud, around 22 K, than in the southern side, around 16 K. In contrast, the NH_3 column density has the highest values in the south of the main cloud. The N_2H^+ column density distribution resembles the dust emission, strong in the northern side of the main cloud. We found three local temperature enhancements which seem to be associated with embedded YSOs, one of them associated with a 2MASS source, and the other two, the Northern Warm Spot and the Southern Warm Spot, associated with faint continuum infrared emission at 2.12 μm.
3. There is strong chemical differentiation in the region. In particular, we found low values of the NH_3/N_2H^+ ratio, ∼50, associated with YSOs, and high values, up to 300, associated with starless cores. This is consistent with NH_3 being enhanced with respect to N_2H^+ at moderate densities ($\lesssim 10^5$ cm^{-3}), while at densities around $\sim 10^6$ cm^{-3} the NH_3 enhancement may be less important (due to shorther lifetimes of the cores), and additionally the effects of NH_3 depletion may start to play a role.
4. We identified three cores in the NH_3 column density map, with low temperatures and with no infrared emission associated, similar to starless cores in low-mass star-forming regions, but with temperatures slightly higher, ∼15 K, possibly due to external heating from the nearby OB stars. These are associated with BIMA 3, BIMA 4, and the western cloud.
5. Interaction between the different sources in the region is important. First, the UCH II region is interacting with the main cloud heating and enhancing the CN (1–0) emission in the edge of the main cloud that is facing the UCH II region. Second, one of the outflows in the region, outflow A, seems to be excavating a cavity and heating its walls. Third, another outflow in the region, outflow B, is interacting with the BIMA 4 starless core, likely producing the deflection of the outflow seen at this position. Such a shock could be illuminating a clump with narrow CH_3OH lines located ∼0.2 pc to the northeast of the shock. We propose that the Northern Warm Spot may contain the driving source of outflow B. The properties of the molecular gas around the outflows suggest that outflow A is more energetic and/or older than outflow B.
6. There are about eight YSOs in the dense gas near the UCH II region. For the YSOs for which we could estimate the associated circumstellar mass, we found values ranging from < 0.4 to ∼4 $M_{\odot}$. In addition, the YSOs seem to be in different

evolutionary stages, even if we consider only the low-mass sources. Thus, stars do not seem to form simultaneously in this cluster environment.

7. While we cannot discard that interaction between the different sources may have triggered star formation in particular cases, triggering cannot explain the overall spatial distribution of the YSOs, suggesting that this may be essentially determined by the initial conditions in the cloud.

Acknowledgements. A. P. is grateful to M. S. Nanda Kumar for providing us the H_2 images, to Maite Beltran and Rosario López for help in technical aspects of this paper, to Serena Viti for chemistry modeling, and to Oscar Morata and the anonymous referee, whose comments and discussions significantly improved the clarity of the paper. The authors A. P., R. E., and J. M. G. are supported by a MEC grant AYA2005-08523 and FEDER funds. H. B. acknowledges financial support by the Emmy-Noether-Program of the Dutsche Forschungsgemeinschaft (DFG, grant BE2578). This publication makes use of data products from the Two Micron All Sky Survey, which is a joint project of the University of Massachusetts and the Infrared Processing and Analysis Center/California Institute of Technology, funded by the National Aeronautics and Space Administration (NASA) and the National Science Foundation.

References

Aikawa, Y., Herbst, E., Roberts, H., & Caselli, P. 2005, ApJ, 620, 330
Aikawa, Y., Ohashi, N., & Herbst, E. 2003, ApJ, 593, 906
Anglada, G., Estalella, R., Mauersberger, R., et al. 1995, ApJ, 443, 682
Bachiller, R., & Pérez Gutiérrez, M. 1997, IAUS, 182, 153
Beltrán, M. T., Girart, J. M., Estalella, R., Ho, P. T. P., & Palau, A. 2002, ApJ, 573, 246
Benson, P. J., Caselli, P., & Myers, P. C. 1998, ApJ, 506, 743
Bernasconi, P. A., & Maeder, A. 1996, A&A, 307, 829
Beuther, H., Schilke, P., Menten, K. M., et al. 2002a, ApJ, 566, 945
Beuther, H., Schilke, P., Menten, K. M., et al. 2005a, ApJ, 633, 535
Beuther, H., Walsh, A., Schilke, P., et al. 2002b, A&A, 390, 289
Beuther, H., Schilke, P., & Gueth, F. 2004a, ApJ, 608, 330
Beuther, H., Schilke, P., & Wyrowsky, F. 2004b, ApJ, 615, 832
Beuther, H., Thorwirth, S., Zhang, Q., et al. 2005b, ApJ, 627, 834
Boger, G. I., & Sternberg, A. 2005, ApJ, 632, 302
Caselli, P., Benson, P., Myers, P. C., & Tafalla, M. 2002, ApJ, 572, 238
Crapsi, A., Caselli, P., Walmsley, C. M., et al. 2005, ApJ, 619, 379
Dyson, J. E., & Williams, D. A. 1997, in *The Physics of the Interstellar Medium*, eds. R. J. Tayler, & M. Elvis, The Graduate Series in Astronomy
Felli, M., Massi, F., Robberto, M., & Cesaroni, R. 2006, A&A, astro-ph/0603818
Fuente, A., Martín-Pintado, J., Cernicharo, J., & Bachiller, R. 1993, A&A, 276, 473
Garay, G., & Lizano, S. 1999, PASP, 111, 1049
Girart, J. M., Estalella, R., Anglada, G., et al. 1997, ApJ, 489, 734
Girart, J. M., Estalella, R., & Ho, P. T. P. 1998, ApJ, 495, L59
Girart, J. M., Rodríguez, L. F., Anglada, G., et al. 1994, ApJ, 435, L145
Girart, J. M., Viti, S., Williams, D. A., Estalella, R., & Ho, P. T. P. 2002, A&A, 388, 1004
Hester, J. J., & Desch, S. J. 2005, in *Chondrites and the Protoplanetary Disk*, eds. A. N. Krot, E. R. D. Scott, & B. Reipurth, p. 107, San Francisco: Astronomical Society of the Pacific,
Hillenbrand, L. A. 1995, PhD Thesis, University of Massachusetts
Hillenbrand, L. A., & Hartmann, L. W. 1998, ApJ, 492, 540
Ho, P. T. P. 1977, PhD Thesis, Massachusetts Institute of Technology
Ho, P. T. P., Peng, Y.-L., Torrelles, J. M., et al. 1993, ApJ, 408, 565
Ho, P. T. P., & Townes 1983, ARA&A, 21, 239
Hotzel, S., Harju, J., & Walmsley, C. M. 2004, A&A, 415, 1065
Jijina, J., Myers, P. C., & Adams, F. C. 1999, ApJSS, 125, 161
Joergensen, J. K. 2004, A&A, 424, 589
Kumar, M.S.N., Bachiller, R., & Davis, C.J. 2002, ApJ, 576, 313
Le Duigou, J.-M. & Knödlseder, J. 2002, A&A, 392, 869
Li, D., Goldsmith, P. F., & Menten, K. 2003, ApJ, 587, 262
Looney, L. W., Wang, S., Hamidouche, M., Safier, P. N., & Klein, R. 2006, astro-ph/0601437
McCaughrean, M. J., & Stauffer, J. R. 1994, AJ, 108, 1382
Moriarty-Schieven, G. H., Johnstone, D., Bally, J., & Jenness, T. 2006, ApJ, 641, astro-ph/0512351
Panagia, N. 1973, AJ, 78, 929
Peretto, N., André, P., & Belloche, A. 2006, A&A, 445, 979
Pirogov, L., Zinchenko, I., Caselli, P., Johansson, L. E. B., & Myers, P. C. 2003, A&A, 405, 639
Sault, R. J., Teuben, P. J., & Wright, M. C. H. 1995, in ASP Conf. Ser. 77, Astronomical Data Analysis Software and Systems IV, ed. R. A. Shaw, H. E. Payne, & J. J. E. Hayes (San Francisco: ASP), 433
Sepúlveda, I. 1993, Master Thesis, University of Barcelona
Simon, R., Stutzki, J., Sternberg, A., & Winnewisser, G. 1997, A&A, 327, L9
Skrutskie, M. F., Cutri, R. M., Stiening, R., et al. 2006, AJ, 131, 1163
Sridharan, T. K., Beuther, H., Schilke, P., Menten, K. M., & Wyrowski, F. 2002, ApJ, 566, 931
Tafalla, M., Myers, P. C., Caselli, P., & Walmsley, C. M. 2004, A&A, 416, 191
Tafalla, M., Myers, P. C., Caselli, P., Walmsley, C. M., & Comito, C. 2002, ApJ, 569, 815
Testi, L., Palla, F., Natta, A. 1998, A&ASS, 133, 81
Testi, L., Palla, F., Natta, A. 1999, A&A, 342, 515
Testi, L., Palla, F., Natta, A. 2000, in *From Darkness to Light*, T. Montmerle & P. André eds., ASP Conference Series
Torrelles, J. M., Rodríguez, L. F., Cantó, J., et al. 1992, ApJ, 396, L95
Walmsley, C. M., & Ungerechts, H. 1983, A&A, 122, 164
Wang, Y., Wu, Y., Zhang, Q., Mao, R.-Q., & Miller, M. 2006, accepted by A&A
Wiseman, J. J., & Ho, P. T. P. 1996, Nature, 382, 139
Yokogawa, S., Kitamura, Y., Momose, M., & Kawabe, R. 2003, ApJ, 595, 266
Zhang, Q., Hunter, T. R., Sridharan, T. K., & Ho, P. T. P. 2002, ApJ, 566, 982